IIETA International Information and Engineering Technology Association
Advancing the World of Information and Engineering

Traitement du Signal
Vol. 41, No. 4, August, 2024, pp. 1899-1910
Journal homepage: http://iieta.org/journals/ts

Alzheimer's Disease Classification Using Wavelet-Based Image Features

Neha Garg[1*], Mahipal Singh Choudhry[1], Rajesh M Bodade[2]

[1] Department of Electronics and Communication, Delhi Technological University, Delhi 110042, India
[2] Military College of Telecommunication Engineering (MCTE), Indore 453441, India

Corresponding Author Email: ngcoolneha@gmail.com

https://doi.org/10.18280/ts.410420

Received: 16 November 2023
Revised: 18 February 2024
Accepted: 29 March 2024
Available online: 31 August 2024

Keywords:
Alzheimer's disease detection, local binary pattern, mild cognitive impairment, principal component analysis, wavelet transform-based method

ABSTRACT

Alzheimer's disease (AD) is a big issue within a population of aged people. AD starts with cognitive decline initially and creates miserable conditions for patients with time. One of the best preventive measures to control AD is its early detection at the Mild Cognitive Impairment (M_iCI) stage. The M_iCI is a transition stage between normal ageing and AD. The M_iCI stage refers to the noticeable decline in cognitive abilities of a patient, that is more pronounced than would be expected for his age but not severe enough to substantially affect his daily life. Early detection at M_iCI stage allows for prompt intervention and medication, which can help manage symptoms more effectively. This paper proposed a new feature extraction technique namely, Wavelet-based Shifted Circular-Elliptical Local Descriptors (WSCELD) for early AD detection. The proposed WSCELD combines the Double-Density Dual-Tree Complex Wavelet Transform (DD-DTCWT) with the shifted elliptical and circular local binary patterns for extracting directional and structural features in terms of multiple micro and macro patterns. The histogram features are obtained from transform domain images using the proposed WSCELD and have been used for classification. Different variants of WSCELD viz. Mean WSCELD, Median WSCELD, Energy WSCELD and Variance WSCELD have been investigated and Energy WSCELD has been proposed. Experimental results show the Energy WSCELD as the best performer with classification accuracy, sensitivity, and specificity of 97.3±1.6%, 97.1±1.2% and 97.2±1.1% for AD/Normal Controls (N_oC) classification, 94.6±1.1%, 96.1±1.2% and 93.1±1.1% for AD/M_iCI classification and 93.8±1.4%, 92.4±1.5% and 96.2±1.2% for M_iCI/N_oC classification respectively. The proposed approach is the automated approach for AD detection and is suitable for clinical implementation for early AD detection.

1. INTRODUCTION

Alzheimer's disease (AD) is a neurological syndrome affecting a large population of early-aged people worldwide. AD results in a continual decline in cognitive and communication skills which makes an individual unable to work without assistance [1]. More than 5 million people in the United States alone, were suffering from AD in 2018, and it is expected that this figure will be 15 million by 2050. The AD is not limited to the US people only, but it is spreading on a large scale across the world. The main reason behind the progression of AD is the accumulation of amyloid and tau proteins in brain regions. This accumulation causes synaptic loss in the brain and results in structural changes in the brain such as ventricular enlargement, hippocampal volume and size variations, cerebral cortex surface contraction, and grey matter density fluctuations [2, 3]. Magnetic Resonance Imaging (MRI) is one of the best neuroimaging tests that captures these structural changes with good tissue contrast and high resolution [4]. This paper presents a new feature extraction technique that extracts directional local descriptors which depict the structural and grey matter density variations at different stages and are helpful in early AD detection.

In literature, most of the studies include AD detection methods based on Voxel-based morphometry (VBM) [5], Surface-Based Morphometry (SBM) [6], Region of Interest (ROI) [7], Transform-based methods [8] and Texture-based methods [9]. VBM technique provides grey matter density details and compares the anatomy of different brains with a template. This technique suffers from the problem of imperfect image registration and misalignment issues of template and image [10]. The SBM provides cortical features but requires skills in the Freesurfer tool. This technique faces challenges in perfect spatial registration and surface reconstruction which affect the reliability of morphometric measurements [11]. ROI-based methods require segmentation to extract the affected part of the brain, and this needs expertise with prior knowledge. Transform-based methods generally suffer from high dimensionality and are less directionally sensitive to 3-D images [11]. Texture-based methods face challenges in clinics due to the lack of standardized approaches for acquiring MR images, performing intensity discretization on MR images, and selecting MRTA software [11]. Liu et al. [12] used the VBM technique to obtain voxel-wise grey matter density maps from different local patches for AD classification. The authors used a single atlas for obtaining patches which is mostly inclined for a particular class. In ROI-based studies [13, 14] hippocampal visual features [13] and tissue-segmented features [14] have been used for AD classification. These techniques provide spatial domain features which are not directional. The recent studies [15-17] are transform domain studies. These studies [15-17] used shearlet transform [15] and contourlet transform [16, 17] to obtain features from different ROIs and density maps for AD classification. These studies [15-17] included the limitations of VBM and ROI-based methods. However, these studies [15-17] provided frequency domain features which show multiscale and directional information. Most of the texture-based studies used local descriptors as features for AD classification. Bhasin et al. [18] applied 3-DWT to obtain Local Binary Pattern-20 (LBP-20) features for AD classification. This technique used DWT which has low directional selectivity in comparison to complex wavelet. Francis and Pandian [19] proposed a feature extraction technique which enhances the effectiveness of a fast Hessian detector by combining it with the local binary pattern. Sarwinda and Bustamam [20] combined 2D and 3D advanced LBP for multi-class classification of Alzheimer's disease. This method suffered from high dimensionality and large computational time. Oppedal et al. [21] combined the LBP texture features with the contrast measures extracted from MR scans and obtained 98% accuracy. Koh et al. [22] applied bidirectional empirical mode decomposition on MR images and obtained four IMFS. The authors computed LBP histograms from these IMFS and further used these histograms for AD classification. Kaplan et al. [23] obtained Histogram-oriented gradients (HOG), local binary pattern (LBP) and local phase quantization (LPQ) from brain images. The authors merged all features and selected optimum features by using Neighbourhood Component Analysis for AD classification. All the discussed techniques [18-23] are texture-based and extract features based on textures only.

This paper instigates an approach that combines the characteristics of transform-domain and texture-domain techniques for extracting features. These features have the characteristics of both spatial domain and frequency domain and thus are more informative. The contribution of the paper can be listed as follows. (1) The proposed method utilizes DD-DTCWT for extracting features in sixteen directions. Thus, the proposed technique provides directional features. (2) This paper proposed a method which utilizes the local descriptors having the properties of both circular and elliptical LBP's. Circular LBP provides isotropic information and Elliptical LBP provides anisotropic information. In tradition, the histograms of CLBP and ELBP need to be concatenated to capture both isotropic and anisotropic details in the image. This increases the feature vector size. In the proposed technique, CELD is used which provides circular and elliptical LBP properties with just half of the feature vector size [24]. (3) The proposed method can be applied for the detection of different stages of AD as it captures both grey matter density fluctuation and multi-structural variations in the brain with the advancement of the disease. Imaginary coefficients capture structural information and detail sub-bands provide information regarding grey matter density fluctuation. (4) This paper uses the shifted version of WSCELD. This contributes to providing several adaptable micro and macro patterns. (5) This paper compares the performance of different versions of WSCELD like Median WSCELD, Mean WSCELD, Energy WSCELD and Variance WSCELD using different wavelets like DD-DWT [25], DTCWT [26] and DD-DTCWT [27].

The remaining paper is divided into three sections as follows. The second section includes the proposed approach with background material. The third section includes the details of the database, performance metrics and performance discussion of the proposed work and existing methods. The fourth section throws light on the conclusion with future directions.

2. PROPOSED METHOD

In the proposed method DD-DTCWT is applied on 2-D MR scans and sixteen high-frequency subbands are obtained at the first level of decomposition. Now Shifted Circular Elliptical Local Descriptors are used to obtain the local micro and macro patterns from the 16 sub-images. Different versions like Median WSCELD, Mean WSCELD, Energy WSCELD and Variance WSCELD have been tested and Energy WSCELD has been proposed for detection of AD at different stages on account of its performance. Figure 1 indicates the block diagram of the proposed methodology.

The LBP [28] detects the geometric features like edges, hard lines, and corners in the images and provides the local spatial structural patterns. These patterns are obtained by generating a binary code for a centre pixel by comparing the neighbouring pixels with the centre pixel value. In CLBP all neighbouring pixels are present on a circle of radius R from the centre pixel. Figure 2 shows the CLBP with a 3x3 neighbourhood. The CLBP value of a pixel Pc (X_{ce}, Y_{ce}) with its N neighbours can be calculated as in Eq. (1).

$$LBP_{N,R}(X_{ce}, Y_{ce})=\sum_{n=1}^{N} \mathrm{Sign}(Y)2^{n-1} \quad (1)$$

Y=Pn(R)-Pc where Pn represents the neighbour pixel at R distance from centre pixel Pc and the value of Y can be assigned 0 and 1 based on Eq. (2).

$$\mathrm{Sign}=\begin{cases}1, Y \geq 0\\ 0, Y < 0\end{cases} \quad (2)$$

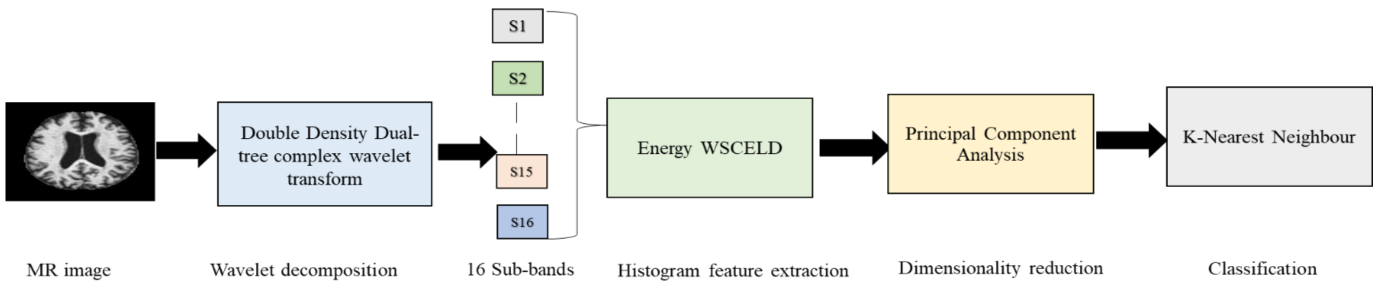

Figure 1. The flow of process in the proposed methodology

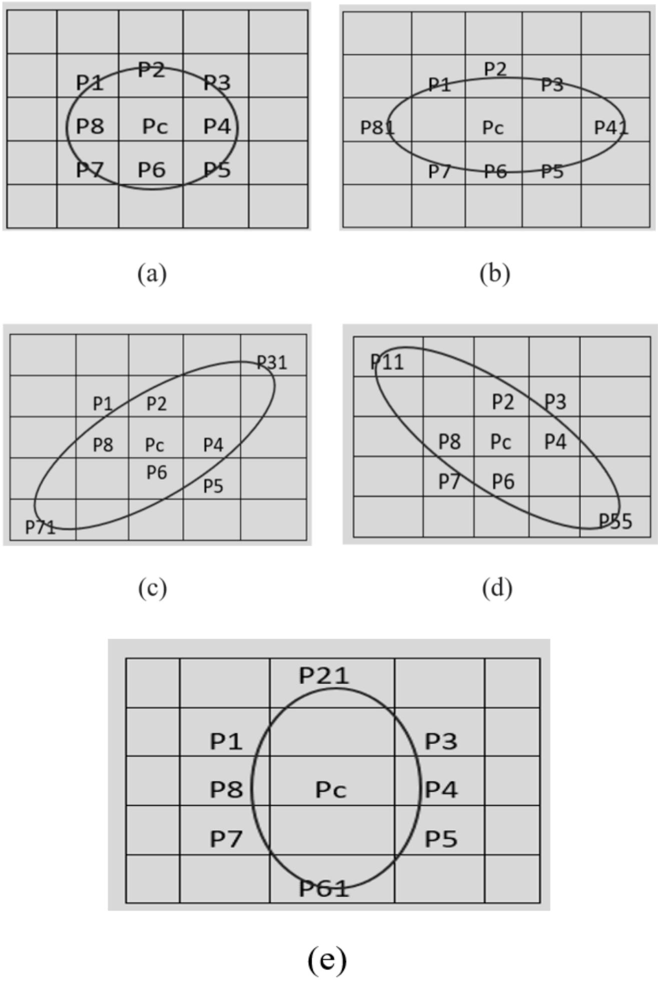

Figure 2. (a) CLBP (b) H-ELBP (c) Right-oriented Diagonal ELBP (d) Left-oriented Diagonal ELBP (e) V-ELBP

The coordinates of N number of neighbours Pn (X_{ne}, Y_{ne}) around the centre pixel are obtained by using Eq. (3) and Eq. (4).

$$X_{ne}=X_{ce}+R\cos(2\pi/N) \quad (3)$$

$$Y_{ne}=Y_{ce}+R\sin(2\pi/N) \quad (4)$$

ELBP [29] considers that neighbouring pixels are in an elliptical pattern around the centre pixel. The ellipse orientation can be diagonal, horizontal, and vertical. The ELBP value of a pixel Pc (X_{ce}, Y_{ce}) with its N neighbours lying on the ellipse of radius R1 horizontally and R2 vertically around it, can be calculated by using Eq. (5).

$$ELBP_{N,R1,R2}(X_{ce}, Y_{ce}) = \sum_{n=1}^{N} \mathrm{Sign}(Y)2^{n-1} \quad (5)$$

Y=Pn (R1, R2)-Pc where Pn represents the neighbour pixel at R1 and R2 horizontal and vertical distance respectively from centre pixel Pc and the value of Y can be assigned 0 and 1 based on Eq. (6).

$$\mathrm{Sign}=\begin{cases}1, Y \geq 0\\ 0, Y < 0\end{cases} \quad (6)$$

The coordinates of N number of neighbours Pn (X_{ne}, Y_{ne}) around the centre pixel are obtained through Eq. (7) and Eq. (8).

$$X_{ne}=X_{ce}+R1\cos(2\pi/N) \quad (7)$$

$$Y_{ne}=Y_{ce}+R2\sin(2\pi/N) \quad (8)$$

Figure 2 shows the different patterns of Circular LBP and Elliptical LBP.

2.1 Circular elliptical local descriptor (CELD)

In the proposed method, CELD extracts isotropic and anisotropic structural details with a small-size feature vector. CELD generates a unique code by thresholding the eight neighbouring points that are needed for circular LBP, horizontal, vertical and diagonal ELBPs around a centre pixel Pc(X_{ce},Y_{ce}). The eight neighbouring points in CELD are taken by combining the two pixels (P2 and P21) at top, two pixels (P6 and P61) at bottom, two pixels (P8 and P81) at left, two pixels (P4 and P41) at right, and four pair of two diagonal pixels (P1 and P11, P5 and P51, P3 and P31, P7 and P71) as shown in Figure 3.

P11		P21		P31
	P1	P2	P3	
P81	P8	Pc	P4	P41
	P7	P6	P5	
P71		P61		P51

(a) Neighbouring points

	(P1+ P11)/2	(P2+ P21)/2	(P3+ P31)/2	
	(P8+ P81)/2	Pc	(P4+ P41)/2	
	(P7+ P71)/2	(P6+ P61)/2	(P5+ P51)/2	

(b) Formulation of neighbouring points in CELD

Figure 3. Eight neighbouring points in CELD

Formulas used in the formulation of 3X3 neighbourhood in eight neighbouring points CELD are mentioned in Eq. (9) to Eq. (12).

$$P1=\mathrm{int}(P1+P11)/2 \quad P2=\mathrm{int}(P2+P21)/2 \quad (9)$$

$$P3=\mathrm{int}(P3+P31)/2 \quad P4=\mathrm{int}(P4+P41)/2 \quad (10)$$

$$P5=\mathrm{int}(P5+P51)/2 \quad P6=\mathrm{int}(P6+P61)/2 \quad (11)$$

$$P7=\mathrm{int}(P7+P71)/2 \quad P8=\mathrm{int}(P8+P81)/2 \quad (12)$$

Based on the above details the CELD can be formulated as in Eq. (13):

$$CELD\ N, R1, R2\ (X_{ce}, Y_{ce})=\sum_{n=1}^{N} \mathrm{Sign}(Y)2^{n-1} \quad (13)$$

where, Y=Pn(R1, R2)–Pc and Pn represents the neighbour pixel and Pc represents the centre pixel and the value of Y can be assigned as 0 and 1 based on the Eq. (14).

$$\text{Sign}=\begin{cases}1, Y \geq 0 \\ 0, Y < 0\end{cases} \tag{14}$$

Here R1 is the radius of circular LBP, the vertical radius of Horizontal ELBP and the horizontal radius of Vertical ELBP; The R2 is the horizontal radius of Horizontal ELBP and the vertical radius of Vertical ELBP.

2.2 Shifted circular elliptical local descriptor (SCELD)

A shifted version of CELD helps in capturing all possible micro and macro patterns which is essential for AD detection. These micropatterns include fine-grained textures and minute differences in local regions of brain images. This can help in detecting atrophies at a cellular or subcellular level, such as changes in neuronal structures and synapse density, or the existence of microscopic lesions. Macro patterns include larger-scale features in brain images which can be obtained by evaluating overall brain structure, locating atrophied regions, and detecting macroscopic atrophies like enlarged ventricles or cortical thinning. The histogram features obtained through shifted CELD provide high structural information and can lead to good classification results.

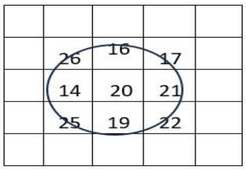

Figure 4. Sample of eight neighbouring points in CELD with centre pixel

Shifted CELD can be obtained by obtaining 8 patterns by using the shifted version shown in Figure 4 and Figure 5. In the proposed work the average CELD value of all patterns has been taken to reduce the computation burden. Eq. (15) to Eq. (24) represent the SCELD.

$$\begin{aligned}\text{SCELD} \cdot N, R1, R2 \cdot \text{Pc}(X_{\text{ce}}, Y_{\text{ce}}) &= [\text{CELD}_{\text{Pattern1}} + \text{CELD}_{\text{Pattern2}} \\ &+ \text{CELD}_{\text{Pattern3}} + \text{CELD}_{\text{Pattern4}} \\ &+ \text{CELD}_{\text{Pattern5}} \\ &+ \text{CELD}_{\text{Pattern6}} + \text{CELD}_{\text{Pattern7}} \\ &+ \text{CELD}_{P_{\text{attern8}}}]/8\end{aligned} \tag{15}$$

where,

$$\text{CELD}_{\text{Pattern1}}=\sum_{n=1}^{N} \text{Sign}(\text{Y1})2^{n-1} \tag{16}$$

$$\text{CELD}_{\text{Pattern2}}=\sum_{n=1}^{N} \text{Sign}(\text{Y2})2^{n-1} \tag{17}$$

$$\text{CELD}_{\text{Pattern3}}=\sum_{n=1}^{N} \text{Sign}(\text{Y3})2^{n-1} \tag{18}$$

$$\text{CELD}_{\text{Pattern4}}=\sum_{n=1}^{N} \text{Sign}(\text{Y4})2^{n-1} \tag{19}$$

$$\text{CELD}_{\text{Pattern5}}=\sum_{n=1}^{N} \text{Sign}(\text{Y5})2^{n-1} \tag{20}$$

$$\text{CELD}_{\text{Pattern6}}=\sum_{n=1}^{N} \text{Sign}(\text{Y6})2^{n-1} \tag{21}$$

$$\text{CELD}_{\text{Pattern7}}=\sum_{n=1}^{N} \text{Sign}(\text{Y7})2^{n-1} \tag{22}$$

$$\text{CELD}_{\text{Pattern8}}=\sum_{n=1}^{N} \text{Sign}(\text{Y8})2^{n-1} \tag{23}$$

where,

Y1=Pn(R1,R2)-Pc Y2=Pn_{+1}(R1,R2)-Pc
Y3=Pn_{+2}(R1,R2)-Pc Y4=Pn_{+3}(R1,R2)-Pc
Y5=Pn_{+4}(R1,R2)-Pc Y6=Pn_{+5}(R1,R2)-Pc
Y7=Pn_{+6} (R1,R2)-Pc Y8=Pn_{+7}(R1,R2)-Pc

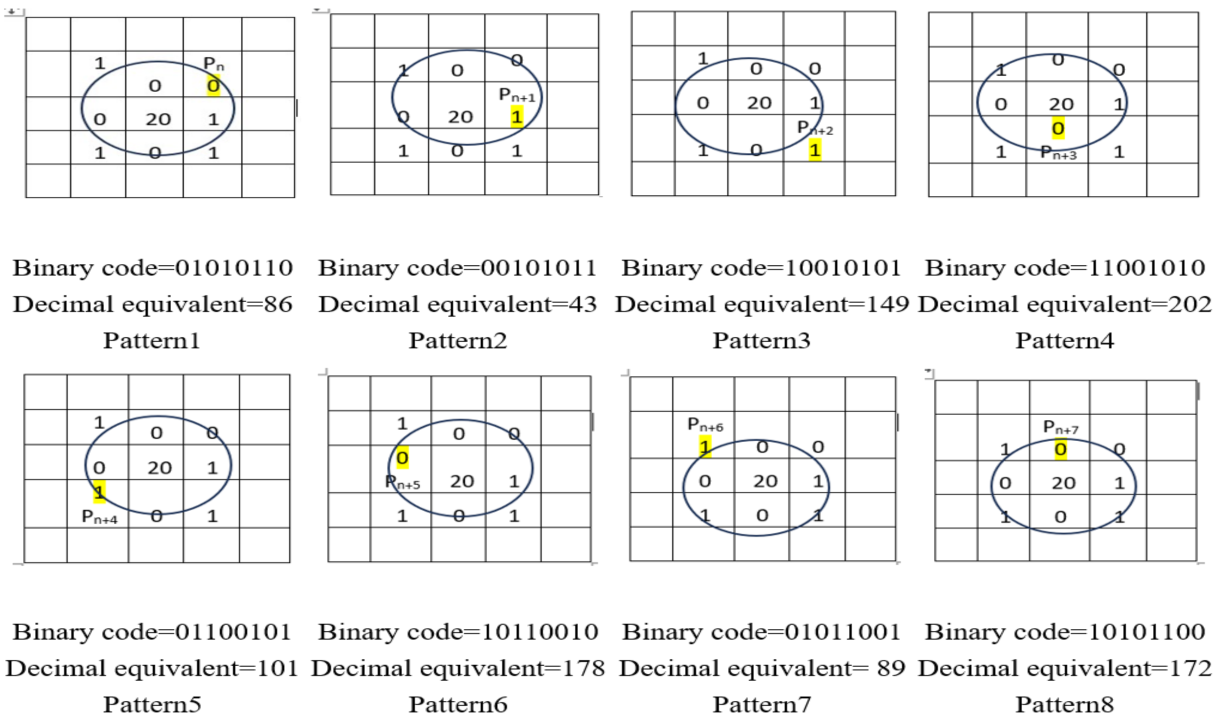

Figure 5. Shifted eight patterns

$$\text{Sign}=\begin{cases}1, Y \geq 0\\ 0, Y < 0\end{cases} \quad (24)$$

SCELD provides 256 histogram bins which represent the average value of histogram bins of 8 shifted patterns.

2.3 Wavelet-based shifted circular elliptical local descriptor (WSCELD)

The combination of SCELD with wavelet results in WSCELD which provides the directional multiple patterns and enhances the classification accuracy. The wavelet transform captures directional information through the decomposition into different subbands, each related to a particular orientation and scale. SCELD applied to each subband independently, captures local texture patterns within each frequency band. The combination of wavelet subbands and SCELD provides a multi-scale representation, allowing the algorithm to analyze structural changes, grey matter density fluctuations and textures at different levels of detail. Eq. (25) to Eq. (29) indicate how the real coefficients of complex wavelets extract average information and imaginary coefficients extract structural information.

Let complex wavelet have $\chi_s(t)=x_s(t)+y_s(t)$ as scaling function and $\varphi_w(t)=u_w(t)+iv_w(t)$ as wavelet function. For scaling function, ratio between $x_s(w)$ and $y_s(w)$ is

$$\lambda_s(w)=-\frac{y_s(w)}{x_s(w)} \quad (25)$$

where, $x_s(w)$ and $y_s(w)$ are Fourier Transform (FT) of $x_s(t)$ and $y_s(t)$ respectively. $\lambda_s(w)$ is surely real-valued and acts as w^2 for $|w| < \pi$ [30]. $y_s(t)$ is approximately equal to the second derivative of $x_s(t)$ multiple by some constant factor.

For wavelet function $\varphi_w(t)$ also, the ratio between $u_w(w)$ and $v_w(w)$ is

$$\varpi_w(w)=-\frac{v_w(w)}{u_w(w)} \quad (26)$$

where, $u_w(w)$ and $v_w(w)$ are FT of $u_w(t)$ and $v_w(t)$ respectively. $\varpi_w(w)$ is also real valued and $v_w(t)$ is approximately equal to the second derivative of $u_w(t)$ multiple by some constant factor.

There exists a relationship between the real component of wavelet function and scaling function as:

$$\zeta(w)=-i\frac{u_w(w)}{x_s(w)} \quad (27)$$

where, $\zeta(w)$ is surely real-valued and acts as w^{m+1} for $|w| < \pi$ [30].

Eq. (25) and Eq. (26) indicate $y_s(t)\approx\lambda_s\Delta x_s(t)$ and $v_w(t)\approx\varpi_w\Delta u_w(t)$. This gives multi-scale projections as:

$$\begin{aligned}\left(s_{si}(t),\chi_{m,k}(t)\right)&=\left(s_{si}(t),x_{m,k}(t)\right)+i\left(s_{si}(t),y_{m,k}(t)\right)\\ &\approx\left(s_{si}(t),x_{m,k}(t)\right)+i\lambda_s\left(s_{si}(t),\Delta x_{m,k}(t)\right)\end{aligned} \quad (28)$$

$$\begin{aligned}\left(s_{si}(t),\varphi_{m,k}(t)\right)&=\left(s_{si}(t),u_{m,k}(t)\right)+i\left(s_{si}(t),v_{m,k}(t)\right)\\ &\approx\left(s_{si}(t),u_{m,k}(t)\right)+i\varpi_w\left(s_{si}(t),\Delta u_{m,k}(t)\right)\end{aligned} \quad (29)$$

where, 'm' and 'k' denote the level of decomposition and orientation respectively. s_{si} is the signal to be decomposed From Eq. (28) and Eq. (29), it can be concluded that the real components of scaling function and wavelet function of complex wavelets sustain averaging information, and the imaginary components of scaling and wavelet function sustain edge information. This average information and edge information play an important role for Alzheimer's disease detection [31]. The high frequency coefficient in detail subbands provide the grey matter density fluctuations which is also essential for AD detection [32].

In the proposed work SCELD has been applied on the sixteen sub-bands obtained by first-level DD-DTCWT decomposition. WSCELD with DD-DTCWT provides directional features from sixteen directions with complete isotropic and anisotropic structural and micro pattern details. The WSCELD with eight neighbours provides histogram bins equal to 256 X number of sub-bands. WSCELD histograms are obtained and have been used for classification. The total number of histogram features with DD-DTCWT is 256 X 16=4096 which is further reduced by using Principal Component Analysis. The different versions of WSCELD like Mean WSCELD, Median WSCELD, Variance WSCELD and Energy WSCELD have been investigated. In Mean WSCELD, Median WSCELD, Variance WSCELD and Energy WSCELD, the centre pixel value is replaced with the mean, median, variance and energy values of the neighbourhood pixels respectively and thresholding of neighbouring pixels is done corresponding to that modified centre pixel. The different versions of WSCELD are shown in Figure 6.

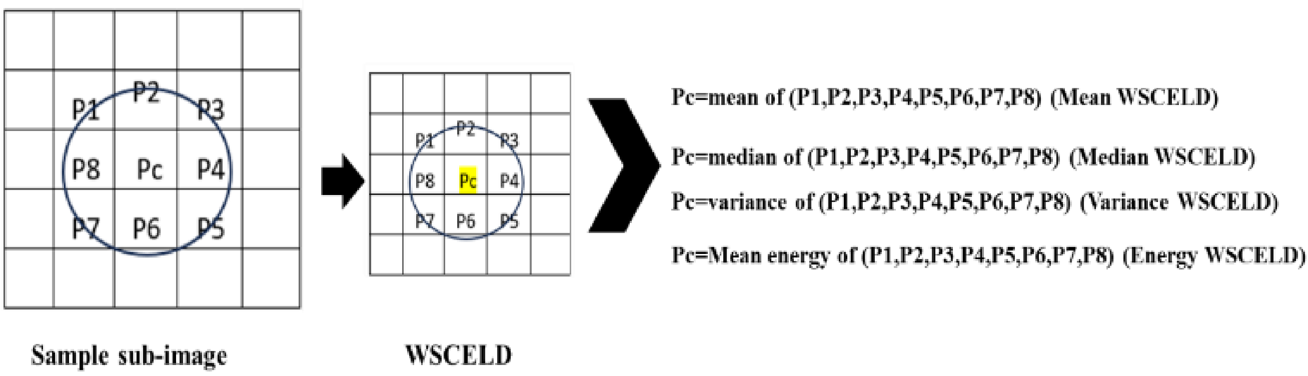

Figure 6. Different versions of WSCELD

3. RESULTS AND DISCUSSION

3.1 Dataset

This study used Open Access Series of Imaging Studies (OASIS) dataset for executing the proposed algorithm [33]. OASIS consists of 3-D MR scans of three categories AD, M_iCI and N_oC having Clinical Dementia Rating (CDR) value of 1,0.5 and 0 respectively. Total 84 3-D MR scans with 28 scans belonging to each category have been obtained for implementation work. Subsequently, 336 MR slices with 112 slices per category are taken out from all 3-D MR scans. These 336 MR slices are the centre slices. The sample images of the centre slices are shown in Figure 7.

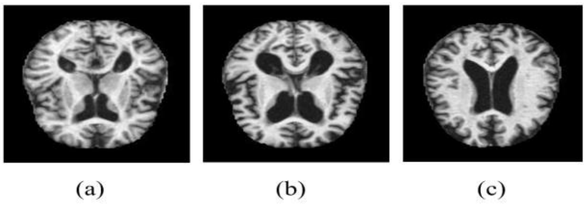

Figure 7. Sample from OASIS dataset (a) Alzheimer's Disease (AD) (b) Mild Cognitive Impairment (M_iCI) (c) Normal Control (N_oC)

3.2 Performance test criteria

The performance of the proposed work is evaluated using three metrics namely, accuracy [34], sensitivity and specificity. These metrics are elaborated in Table 1. In Table 1 T_eP_s denotes true positive, T_eN_g denotes true negative, F_sP_s denotes false positive and F_sN_g denotes false negative. T_eP_s are the total AD individuals precisely detected into AD category, T_eN_g are the total normal subjects precisely detected into normal category, F_sP_s are the total normal subjects wrongly classified into AD category and F_sN_g are the total AD subjects wrongly classified into normal category.

Table 1. Performance criteria

Metrics	Description	Formula
Accuracy(Acc)	effectuality of classifiers to provide right detections out of total outcomes.	$\frac{(T_eP_s + T_eN_g)}{(T_eP_s + F_sN_g + T_eN_g + F_sP_s)}$
Sensitivity(Sen)	effectuality of classifiers to provide right detections for true positives.	$\frac{(T_eP_s)}{(T_eP_s + F_sN_g)}$
Specificity(Spec)	effectuality of classifiers to provide right detections for true negatives.	$\frac{(T_eN_g)}{(T_eN_g + F_sP_s)}$

3.3 Performance comparison of different versions of SCELD with different wavelets for AD/N_oC, M_iCI/N_oC and AD/M_iCI classifications

Different versions of WSCELD have been tested in this work to evaluate the efficacy of the proposed method. The version DD-DTCWT+Energy-SCELD+PCA gives the best results among different versions. The reason is that DD-DTCWT shows higher directional selectivity than DD-DWT and DTCWT. The DD-DTCWT extracts features in sixteen directions while DD-DWT in eight directions and DTCWT in six directions. DD-DTCWT provides more efficient and directional features than DTCWT and DD-DWT.

The energy version of WSCELD outperforms other versions as it captures the energy contribution of the neighbouring pixels. Energy is the most promising parameter for finding structural changes in an image. The structural changes can be monitored through edge detection. Edges show the transformation between textured or smoothed regions and provide significant details about the position and morphological structure of pictured objects [35]. At edges, energy becomes maximum due to the rapid change in pixel values at its orthogonal direction. The ability of energy to capture edges lies in its emphasis on regions with high gradient magnitude or sharp transition in pixel values, indicating the presence of an edge. The squared gradient or energy of an image is an effective way to identify regions with abrupt changes in intensity, making it a key idea for edge detection [36, 37]. The other version like variance captures the local contrast information, the median captures the middle value of neighbouring pixels, and the mean captures the average value of neighbouring pixels. All these versions do not capture fine structural details thus leading to low performance. Table 2 indicates the performance of different versions of SCELD using a decision tree classifier with different wavelets. Table 3 indicates the p-value for the student t-test performed for the accuracy of different groups implemented in Table 2. The groups having p value greater than 0.05 are marked by *. These groups are H-V-ELBP/SCLD, H-V-ELBP/S-H-V-ELBP and SCELD/Mean-SCELD. They do not show significant improvement. However, the proposed version DD-DTCWT+Energy-SCELD+PCA gives outstanding results. The p-value obtained for the proposed version with other implemented versions is less than 0.05 in each case for AD classification. Energy SCELD is the best performer among variance, mean and median, whatever may be the wavelet and the best results are with DD-DTCWT. This shows the efficacy of the proposed method for early AD detection.

It can be observed from Table 2 that Circular Local Binary Pattern (CLBP) provides 84.2±1.4%, 83.2±1.4% and 81.5±1.2% classification accuracy for AD/N_oC, AD/M_iCI, and M_iCI/N_oC classifications respectively. These figures get improved by using Horizontal and Vertical Elliptical Local Binary Patterns (H-V-ELBP) because ELBP captures directional information also. The p-value obtained for group CLBP/H-V-ELBP is 2.60E-04 in Table 3 which is less than 0.05 and shows significant improvement for AD/N_oC classification. Shifted Circular Local Descriptors (SCLD) adds the shifted version in CLBP performance, so results get enhanced due to the contribution of different patterns. The p-value for the group CLBP/SCLD is 0.012 which shows significant improvement in SCLD. Shifted Circular Elliptical Local Descriptors (SCELD) further add the directional patterns thus improving the classification accuracy. Mean-SCELD, Median-SCELD, Energy-SCELD and Variance SCELD are the different versions of SCELD. The performance of Energy -SCELD is outstanding. The p-value for all groups from 7 to 10 in Table 3 is less than 0.05, which shows the significant improvement by Energy SCELD.

Table 2. Performance of different SCELD versions with different wavelets

Methods	AD/N_oC			AD/M_iCI			M_iCI/N_oC		
	Acc	Sen	Spec	Acc	Sen	Spec	Acc	Sen	Spec
CLBP	84.2±1.4	85.6±1.2	83.1±1.1	83.2±1.4	84.1±1.2	82.9±1.1	81.5±1.2	80.1±1.1	82.1±0.9
H-V-ELBP	87.1±1.3	88.1±1.1	86.5±1.2	85.2±0.8	87.0±1.1	83.0±1.1	83.1±1.2	81.5±1.3	85.5±1.5
SCLD	86.3±1.8	87.3±1.4	85.5±1.1	84.7±1.4	82.1±1.2	86.2±1.6	83.5±1.5	84.0±1.3	82.2±1.3
S-H-V-ELBP	87.4±1.5	88.9±1.2	86.5±1.1	85.1±1.2	85.1±1.4	85.5±1.2	83.3±1.3	85.1±1.2	81.9±1.1
SCELD	89.7±1.6	88.1±1.2	90.7±1.2	86.7±1.3	84.1±0.9	88.0±1.2	84.5±1.7	88.3±1.5	80.0±1.4
Mean-SCELD	89.3±1.7	88.5±1.3	91.1±1.1	86.3±1.2	86.2±1.2	85.0±1.3	84.8±1.7	85.5±1.4	83.5±1.5
Median-SCELD	86.4±1.1	86.1±1.1	87.7±1.2	82.6±1.1	81.2±0.8	83.9±1.3	81.3±1.1	79.4±1.2	83.5±1.2
Energy-SCELD	91.6±1.7	92.2±1.4	89.9±1.2	88.0±1.2	91.1±1.1	85.2±0.9	86.3±1.4	88.1±1.1	84.3±0.9
Variance-SCELD	85.4±1.1	87.5±1.2	83.2±1.5	80.5±1.2	80.0±1.4	80.1±1.3	79.2±1.1	78.2±1.2	80.3±1.3
DD-DWT+SCELD+PCA	91.2±1.2	92.5±1.3	90.5±1.1	88.3±1.3	85.1±1.2	91.2±0.8	86.1±1.7	88.5±1.2	84.6±1.1
DD-DWT+Mean-SCELD+PCA	91.9±1.7	92.1±1.1	90.1±1.2	87.6±1.3	87.1±1.1	88.1±1.2	85.1±1.3	88.2±1.1	82.2±1.2
DD-DWT+Median-SCELD+PCA	90.5±0.8	92.5±1.1	88.5±1.2	85.1±1.3	87.1±1.2	83.2±0.9	84.0±1.4	85.1±1.3	83.2±1.3
DD-DWT+Energy-SCELD+PCA	93.5±1.5	90.1±1.2	96.5±1.5	90.0±1.3	89.1±0.9	90.1±1.1	87.6±0.9	84.2±1.1	91.1±1.2
DD-DWT+Variance-SCELD+PCA	89.1±1.2	88.2±0.9	91.2±1.1	85.2±0.8	81.1±1.1	89.2±1.2	83.9±1.3	82.1±1.1	84.2±1.2
DTCWT+SCELD+PCA	94.0±1.3	93.1±1.1	95.5±1.2	89.5±1.1	88.5±1.2	91.5±1.1	88.7±1.3	89.5±1.1	87.1±1.2
DTCWT+Mean-SCELD+PCA	94.2±1.4	95.9±1.2	93.1±1.1	89.2±1.1	90.1±1.1	88.9±0.9	88.3±1.2	87.1±1.1	89.5±1.2
DTCWT+Median-SCELD+PCA	92.7±1.7	94.2±1.5	91.0±1.2	89.1±1.7	90.1±1.2	89.9±1.1	87.7±1.3	89.5±1.4	85.1±1.1
DTCWT+Energy-SCELD+PCA	95.4±0.8	92.2±1.2	98.5±1.1	91.6±1.3	92.5±1.1	90.5±0.9	90.6±1.3	91.9±1.1	89.5±1.2
DTCWT+Variance-SCELD+PCA	91.1±1.3	90.1±1.1	89.5±1.2	88.7±1.8	89.5±1.2	87.5±1.1	86.2±1.3	85.5±1.4	87.5±1.1
DD-DTCWT+SCELD+PCA	95.2±1.3	96.2±1.4	94.3±1.5	92.1±0.9	93.1±1.3	91.5±1.2	92.0±1.3	91.1±1.2	93.5±1.4
DD-DTCWT+Mean-SCELD+PCA	95.0±1.2	94.4±1.2	96.2±1.1	92.6±0.9	91.6±1.1	90.4±1.1	92.5±1.2	94.2±1.1	90.1±1.2
DD-DTCWT+Median-SCELD+PCA	94.3±1.2	94.1±1.1	93.9±1.1	92.1±0.9	94.2±1.1	90.1±1.1	92.0±1.1	96.5±1.4	88.5±1.2
DD-DTCWT+Energy-SCELD+PCA [PROPOSED]	**97.3**±1.6	**97.1**±1.2	**97.2**±1.1	**94.6**±1.1	**96.1**±1.2	**93.1**±1.1	**93.8**±1.4	**92.4**±1.5	**96.2**±1.2
DD-DTCWT+Variance-SCELD+PCA	93.4±1.2	94.1±1.1	92.2±1.2	91.1±0.9	90.2±1.1	92.1±1.5	89.7±1.3	90.5±1.2	88.5±1.2

Table 3. p-value for the t-test performed for the accuracy of different implemented versions in the paper

S.N.	GROUPS	AD/NoC	AD/M_iCI	M_iCI/N_oC
1	CLBP/H-V-ELBP	2.60E-04	2.22E-04	0.015
2	CLBP/SCLD	0.012	0.024	0.005
3	H-V-ELBP/SCLD*	0.340*	0.075*	0.465*
4	H-V-ELBP/S-H-V-ELBP*	0.608*	0.330*	0.919*
5	S-H-V-ELBP/SCELD	0.004	0.025	0.048
6	SCELD/Mean-SCELD*	0.599*	0.848*	0.705*
7	SCELD/Energy-SCELD	0.017	0.042	0.022
8	Mean-SCELD/Energy-SCELD	0.007	0.024	0.049
9	Median-SCELD/Energy-SCELD	7.25E-07	2.37E-08	1.89E-07
10	Variance-SCELD/Energy-SCELD	7.63E-08	1.96E-10	1.22E-09
11	SCELD/DD-DWT-SCELD+PCA	2.74E-02	0.014	0.030
12	DD-DWT-SCELD+PCA/DD-DWT+Energy-SCELD+PCA	2.00E-03	0.014	0.007
13	Energy-SCELD/DD-DWT+ Energy- SCELD+PCA	2.03E-02	0.008	0.035
14	DD-DWT+Mean-SCELD+PCA/DD-DWT+ Energy-SCELD+PCA	4.52E-02	0.008	2.15E-04
15	DD-DWT+Median-SCELD/DD-DWT+Energy-SCELD+PCA	1.29E-04	0.008	7.04E-06
16	DD-DWT+Variance-SCELD/DD-DWT+Energy-SCELD+PCA	2.50E-06	8.61E-07	1.78E-06
17	DD-DWT-SCELD+PCA/DTCWT-SCELD+PCA	1.36E-04	0.041	3.49E-04
18	DTCWT-SCELD+PCA/DTCWT+Energy-SCELD+PCA	0.014	0.002	0.003
19	DD-DWT+Energy-SCELD+PCA/DTCWT+Energy-SCELD+PCA	0.005	0.027	2.12E-05
20	DTCWT+Mean-SCELD+PCA/DTCWT+Energy-SCELD+PCA	0.039	0.041	8.08E-04
21	DTCWT+ Median-SCELD+PCA/DTCWT+Energy-SCELD+PCA	0.0006	0.002	1.04E-04
22	DTCWT+ Variance-SCELD+PCA/DTCWT+Energy-SCELD+PCA	4.21E-07	8.92E-04	7.86E-07
23	DTCWT-SCELD+PCA/DD-DTCWT-SCELD+PCA	3.94E-02	3.46E-05	1.69E-05
24	DTCWT+Energy-SCELD+PCA/DD-DTCWT+Energy-SCELD+PCA	0.007	7.06E-05	5.82E-05
25	DD-DTCWT+Variance-SCELD+PCA/DD-DTCWT+Energy-SCELD+PCA	1.75E-05	2.01E-06	3.42E-06
26	DD-DTCWT+Mean-SCELD+PCA/DD-DTCWT+Energy-SCELD+PCA	0.003	0.004	0.050
27	DD-DTCWT+Median-SCELD+PCA/DD-DTCWT+Energy-SCELD+PCA	3.20E-04	2.28E-04	0.007

In all these models, histograms are used as features, so the number of textural features is 256 in each version. The model DD-DWT+SCELD+PCA combines SCELD with DD-DWT which gives 8 detail sub-bands on wavelet decomposition. SCELD is applied on each detail sub-band and subsequently each sub-band provides 256 textural features. This results in a total number of features of 256X8=2048. In the next step, Principal Component Analysis (PCA) is used to minimize the dimensionality problem. This model gives 91.2±1.2%, 88.3±1.3% and 86.1±1.7% for AD/N_oC, AD/M_iCI, and M_iCI/N_oC classifications respectively. Different versions of DD-DWT+SCELD like mean, median, variance and energy have been tested and the maximum results are obtained with the energy version. The p-value for all groups from 12 to 16 in Table 3 is less than 0.05 which shows the significant improvement by DD-DWT+Energy SCELD. The proposed methodology has been evaluated with three wavelets namely DD-DWT, DTCWT and DD-DTCWT. DTCWT gives 6 high-frequency sub-bands and DD-DTCWT gives 16 high-frequency sub-bands on wavelet decomposition. Thus, the number of histogram features with DTCWT and DD-DTCWT will be 256×6=1536 and 256×16=4096 respectively. Further PCA has been used to reduce dimensionality. Among all three wavelets, the best results are with DD-DTCWT and version DD-DTCWT+Energy-SCELD+PCA giving maximum results of 97.3±1.6%, 94.6±1.1% and 93.8±1.4% with AD/N_oC, AD/M_iCI, and M_iCI/N_oC classifications respectively. The p-value from groups 24 to 27 in Table 3 is less than 0.05 which shows the significance of improvement by DD-DTCWT+Energy-SCELD+PCA for AD classification at all stages. The Receiver Operating Characteristic (ROC) curve of different versions implemented in the paper is shown in Figure 8.

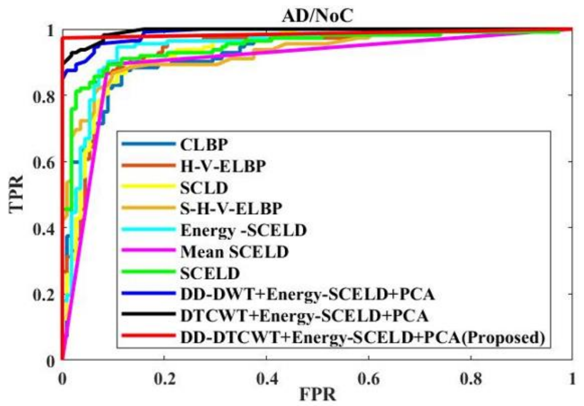

(a) AD/N_oC

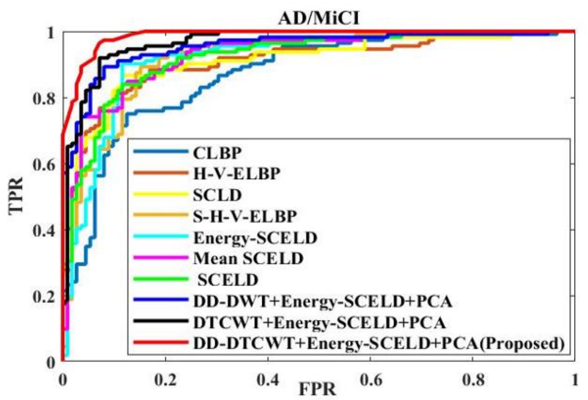

(b) AD/M_iCI

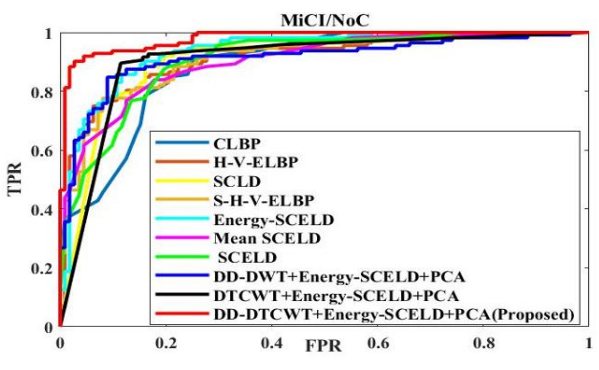

(c) M_iCI/N_oC

Figure 8. ROC plot for different implemented versions

Table 4. Performance of different classifiers

Classifiers	Acc	Sen	Spec
DT	97.3	97	97
KNN	94.1	96	92
NB	87.1	88	87
LSVM	95.1	92	98

Results have been also checked with other classifiers like K-Nearest Neighbour (K-NN), Naive-Bayes (NB) and Linear Support Vector Machine (LSVM). The result of different classifiers with the proposed version is listed in Table 4 and in Figure 9.

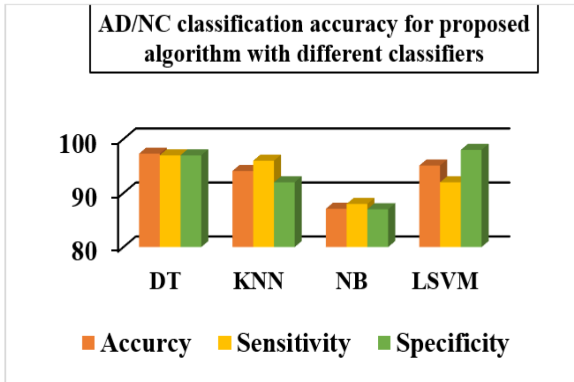

Figure 9. Bar Plot of performance of different classifiers for the proposed version

3.4 Proposed and existing algorithms: Comparative analysis

The proposed method provides outstanding results in terms of accuracy, sensitivity, and specificity. These figures are 97.3±1.6%, 97.1±1.2% and 97.2±1.1%, 94.6±1.1%, 96.1±1.2% and 93.1±1.1% and 93.8±1.4%, 92.4±1.5% and 96.2±1.2% for AD/N_oC, AD/M_iCI, and M_iCI/N_oC classifications respectively. The proposed method has been compared with nine existing methods. The existing methods belong to the different types of AD detection techniques available in literature like wavelet transform-based techniques [38, 39], VBM techniques [12], ROI-based techniques [13, 14] and Texture-based techniques [19]. The proposed and existing methods have been executed ten times on MATLAB-19 using a 10-fold cross-validation technique and their average results are mentioned in Table 5.

The study [38] used DTCWT coefficients as features. This method of execution provides classification accuracy of 88.2±1.1%, 80.2±1.4% 82.0±1.6% for AD/N_oC, AD/M_iCI, and M_iCI/N_oC classifications respectively. The study [39] extracted statistical features by using the combination of DTCWT and its rotated version. This method of execution provides classification accuracy of 90.4±1.1%, 89.7±0.9% and 85.3±1.1% for AD/N_oC, AD/M_iCI, and M_iCI/N_oC classifications respectively. High dimensionality is the main limitation of studies [38, 39]. The study [12] used the VBM technique to select the appropriate grey density maps. A single atlas has been used in the study [12] which is mostly biased. This method of execution provides classification accuracy of 89.3±1.3%, 81.7±1.0% and 83.5±1.2% for AD/N_oC, AD/M_iCI, and M_iCI/N_oC classifications respectively. The studies [13] and [14] belong to ROI based technique as features are extracted from segmented hippocampus [13] and grey matter tissues [14] for AD classification. The study [13] on execution provides 85.3±1.3%, 74.2±1.8%, and 78.1±1.0% and the study [14] provides 88.5±1.2%, 86.2±1.6%, and 85.3±1.3% for AD/N_oC, AD/M_iCI, and M_iCI/N_oC classifications respectively. These studies [13, 14] need a high level of accuracy in segmentation. The recent study [40] is based on a deep learning approach and provides 86.7±1.2%, 83.5±1.6%, and 82.4±1.0% accuracy for AD/N_oC, AD/M_iCI, and M_iCI/N_oC classifications respectively. The p values obtained after performing t-tests on different groups of existing and proposed methods are illustrated in Table 6. Figure 10 indicates the ROC plot of proposed and existing algorithms for AD/N_oC, AD/M_iCI and M_iCI/N_oC classifications.

Table 5 states that the proposed method is 4.8% higher in accuracy for AD/N_oC classification, 3.3% for AD/M_iCI classification and 5.0% for M_iCI/N_oC classification compared to the best-performing existing method. The t-test has also been performed to check the significance of improvement. The p-value for all nine groups mentioned in Table 6 is less than 0.05 which shows the significance of improvement in the proposed technique in comparison to existing techniques.

The proposed technique extracts more informative features which can reflect both structural changes and grey matter density fluctuations. The combined strength of complex wavelet with SCELD helps in extracting structural details and grey matter density variations at a very minute level and thus, improves the classification accuracy. The proposed technique provides outstanding results for classifications at different stages of AD and gives more efficient results for early AD detection. The proposed technique is an automated technique for AD detection with more reliable results. Moreover, the proposed technique has been applied to the whole brain to capture the overall changes in the brain at different stages.

Table 5. Performance comparison of proposed and existing algorithms

Methods	Classifier	AD/N_oC			AD/M_iCI			M_iCI/N_oC		
		Acc	Sen	Spec	Acc	Sen	Spec	Acc	Sen	Spec
Proposed	**KNN**	**97.3±1.6**	**97.1±1.2**	**97.2±1.1**	**94.6±1.1**	**96.1±1.2**	**93.1±1.1**	**93.8±1.4**	**92.4±1.5**	**96.2±1.2**
DTCWT+PCA+LDA [38] [2018]	ELM	88.2±1.1	86.5±1.1	84.4±1.2	80.2±1.4	78.4±1.2	82.3±1.1	82.0±1.6	79.3±1.5	85.1±1.1
LBP-Hessian detector [19] [2021]	CNN	87.5±1.3	89.0±1.0	86.0±1.1	86.3±1.7	83.1±1.5	89.5±1.5	71.5±1.8	72.2±1.4	71.0±1.5
VBM-CT [16] [2021]	SVM	81.3±1.1	83.3±0.9	79.2±1.2	78.8±1.4	83.0±1.5	73.0±1.4	80.4±1.2	82.1±1.1	79.1±1.1
Hippocampus-Visual Features [13] [2015]	SVM	85.3±1.3	77.1±1.3	94.1±1.4	74.2±1.8	75.1±1.5	73.0±1.5	78.1±1.0	77.2±1.2	79.5±1.2
VBM-GM [12] [2012]	SVM	89.3±1.3	87.0±1.2	91.2±1.1	81.7±1.0	84.0±1.1	78.1±1.2	83.5±1.2	88.2±1.1	79.2±1.1
Tissue-Segmentation-based method [14] [2015]	SVM	88.5±1.2	89.5±1.1	87.0±1.2	86.2±1.6	87.1±1.1	86.0±0.9	85.3±1.3	86.2±1.2	85.2±1.1
Deep Learning-VGG16 Feature Extractor [40] [2022]	NN	86.7±1.2	85.2±1.1	87.3±1.0	83.5±1.6	83.0±1.1	84.1±1.2	82.4±1.0	84.1±1.2	80.4±1.0
DTCWT+DTRCWT [39] [2021]	FNN	90.4±1.1	91.2±1.1	89.4±1.0	89.7±0.9	88.2±1.2	91.0±1.1	85.3±1.1	86.1±0.9	84.0±1.1
3D-DWT+LBP-TOP [18] [2020]	SVM	92.8±1.7	94.0±1.0	90.0±1.1	91.5±1.3	92.1±0.9	91.1±1.5	89.3±1.3	84.2±1.2	95.1±1.0

Table 6. p-values for the t-test performed for the accuracy of the proposed method and existing methods

Group	Existing Methods/Proposed	AD/N_oC	AD/M_iCI	M_iCI/N_oC
1	DTCWT+PCA+LDA [38]/Proposed	1.07E-10	1.12E-14	1.52E-12
2	LBP-Hessian detector [19]/Proposed	3.61E-11	1.48E-09	6.20E-16
3	VBM-CT [16]//Proposed	1.28E-14	8.90E-16	2.25E-14
4	Hippocampus-Visual Features [13]/Proposed	1.39E-12	3.64E-15	2.48E-15
5	VBM-GM [12]/Proposed	8.14E-10	3.70E-15	1.88E-12
6	Tissue-Segmentation-based method [14]/Proposed	1.53E-10	3.82E-10	4.88E-11
7	Deep Learning-VGG16 Feature Extractor [40]/Proposed	8.22E-12	5.37E-12	3.54E-13
8	DTCWT+DTRCWT [39]/Proposed	6.46E-09	2.22E-08	3.56E-11
9	3D-DWT+LBP-TOP [18]/Proposed	1.73E-05	4.95E-05	9.58E-07

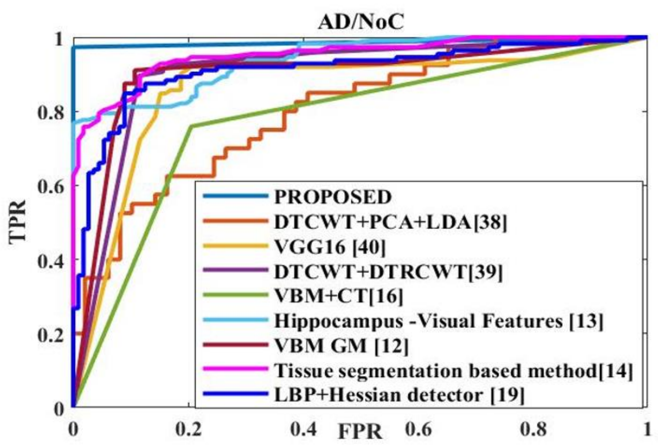

(a) AD/ N_oC

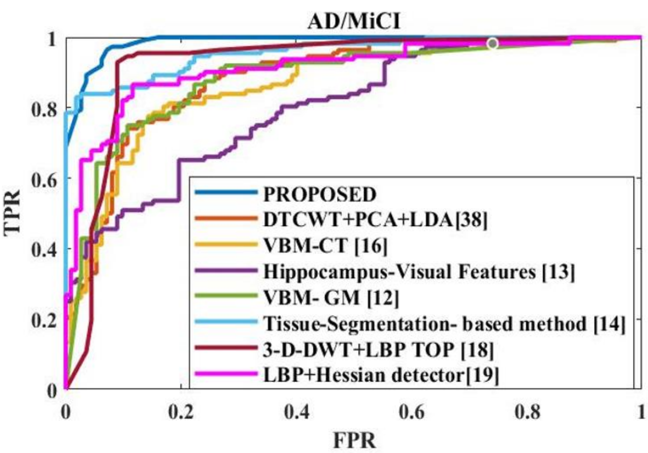

(b) AD/M_ICI

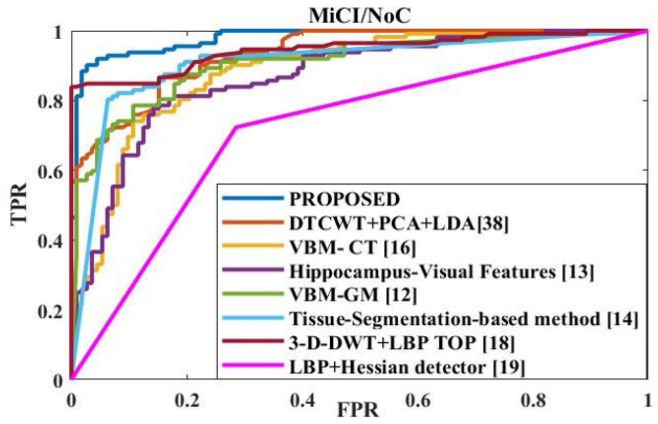

(c) M_iCI/N_oC

Figure 10. ROC plot of proposed and existing methods

4. CONCLUSION

The proposed technique significantly adds the strength of complex wavelets with SCELD and performs remarkably for early AD detection. The proposed Energy WSCELD provides the highest classification accuracy of 97.3±1.6% for AD/N_oC classification,94.6±1.1% for AD/M_iCI classification and 93.8±1.4% for M_iCI/N_oC classification. The proposed method contributes more in comparison to existing methods as it extracts both structural and grey matter density fluctuations while existing techniques focus on capturing a single biomarker for AD detection. Moreover, it does not require segmentation and image registration processes as required in ROI-based and VBM-based techniques. In ROI-based methods, it is difficult to perform accurate segmentation due to the complex structure of the brain and in VBM-based techniques, it is difficult to perform the perfect alignment of images on templates due to the different anatomy of an individual's brain. The proposed method provides frequency domain and spatial domain features while existing techniques provide either frequency domain or spatial domain features.

Alzheimer's classification system helps in drug development, clinical trials and understanding the heterogeneity of Alzheimer's and its underlying mechanism. The impact of the Alzheimer's classification system extends beyond the clinic, influencing public health strategies, research endeavours, and societal support systems. The proposed method is an automated method for Alzheimer's classification and can be used for clinical trials. The proposed technique used histogram features which are high in dimensionality. In future statistical features can be used for AD classification as they provide ease of interpretation, robustness to outliers and memory and computational efficiency. The 2-D wavelet analysis treats each slice of a 3D volume independently, ignoring the potential inter-slice correlations in volumetric data. This may result in the loss of information regarding structures in MR images that span multiple slices. Future work can be focussed on 3-D MR images using 3-D wavelets. In addition, a feature selection stage may be introduced to improve the classification performance.

ACKNOWLEDGMENT

This work is supported by Delhi Technological University, Department of Electronics and Communication, Delhi, India.

REFERENCES

[1] Liu, J., Li, M., Lan, W., Wu, F.X., Pan, Y., Wang, J. (2016). Classification of Alzheimer's disease using whole brain hierarchical network. IEEE/ACM Transactions on Computational Biology and Bioinformatics, 15(2): 624-632. https://doi.org/10.1109/TCBB.2016.2635144

[2] Zhang, J., Gao, Y., Gao, Y., Munsell, B.C., Shen, D. (2016). Detecting anatomical landmarks for fast Alzheimer's disease diagnosis. IEEE Transactions on Medical Imaging, 35(12): 2524-2533. https://doi.org/10.1109/TMI.2016.2582386

[3] Tang, X., Holland, D., Dale, A.M., Younes, L., Miller, M.I., Alzheimer's Disease Neuroimaging Initiative (2014). Shape abnormalities of subcortical and ventricular structures in mild cognitive impairment and Alzheimer's disease: Detecting, quantifying, and predicting. Human Brain Mapping, 35(8): 3701-3725. https://doi.org/10.1002/hbm.22431

[4] Frisoni, G.B., Fox, N.C., Jack, C.R., Jr, Scheltens, P., Thompson, P.M. (2010). The clinical use of structural MRI in Alzheimer disease. Nature Reviews. Neurology, 6(2): 67-77. https://doi.org/10.1038/nrneurol.2009.215

[5] Khagi, B., Lee, K.H., Choi, K.Y., Lee, J.J., Kwon, G.R., Yang, H.D. (2021). VBM-based Alzheimer's disease detection from the region of interest of T1 MRI with supportive Gaussian smoothing and a Bayesian regularized neural network. Applied Sciences, 11(13): 6175. https://doi.org/10.3390/app11136175

[6] de Mendonça, L.J.C., Ferrari, R.J. (2023). Alzheimer's disease classification based on graph kernel SVMs constructed with 3D texture features extracted from MR images. Expert Systems with Applications, 211: 118633. https://doi.org/10.1016/j.eswa.2022.118633

[7] Kubota, T., Ushijima, Y., Nishimura, T. (2006). A region-of-interest (ROI) template for three-dimensional stereotactic surface projection (3D-SSP) images: Initial application to analysis of Alzheimer disease and mild cognitive impairment. International Congress Series, 1290: 128-134. https://doi.org/10.1016/j.ics.2005.11.104

[8] Jha, D., Kim, J.I., Kwon, G.R. (2017). Diagnosis of Alzheimer's disease using dual-tree complex wavelet transform, PCA, and feed-forward neural network. Journal of Healthcare Engineering. https://doi.org/10.1155/2017/9060124

[9] Feng, F., Wang, P., Zhao, K., Zhou, B., Yao, H., Meng, Q., Liu, Y. (2018). Radiomic features of hippocampal subregions in Alzheimer's disease and amnestic mild cognitive impairment. Frontiers in Aging Neuroscience, 10: 290. https://doi.org/10.3389/fnagi.2018.00290

[10] Astrakas, L.G., Argyropoulou, M.I. (2010). Shifting from region of interest (ROI) to voxel-based analysis in human brain mapping. Pediatric Radiology, 40: 1857-1867. https://doi.org/10.1007/s00247-010-1677-8

[11] Garg, N., Choudhry, M.S., Bodade, R.M. (2023). A review on Alzheimer's disease classification from normal controls and mild cognitive impairment using

structural MR images. Journal of Neuroscience Methods, 384: 109745. https://doi.org/10.1016/j.jneumeth.2022.109745

[12] Liu, M., Zhang, D., Shen, D. (2012). Ensemble sparse classification of Alzheimer's disease. Neuroimage, 60(2): 1106-1116. https://doi.org/10.1016/j.neuroimage.2012.01.055

[13] Ben Ahmed, O., Benois-Pineau, J., Allard, M., Ben Amar, C., Catheline, G., Alzheimer's Disease Neuroimaging Initiative. (2015). Classification of Alzheimer's disease subjects from MRI using hippocampal visual features. Multimedia Tools and Applications, 74: 1249-1266. https://doi.org/10.1007/s11042-014-2123-y

[14] Khedher, L., Ramírez, J., Górriz, J.M., Brahim, A., Segovia, F., Alzheimer′s Disease Neuroimaging Initiative. (2015). Early diagnosis of Alzheimer′ s disease based on partial least squares, principal component analysis and support vector machine using segmented MRI images. Neurocomputing, 151: 139-150. https://doi.org/10.1016/j.neucom.2014.09.072

[15] Feng, J., Zhang, S.W., Chen, L., Zuo, C., Alzheimer's Disease Neuroimaging Initiative. (2022). Detection of Alzheimer's disease using features of brain region-of-interest-based individual network constructed with the sMRI image. Computerized Medical Imaging and Graphics, 98: 102057. https://doi.org/10.1016/j.compmedimag.2022.102057

[16] Feng, J., Zhang, S.W., Chen, L. (2021). Extracting ROI-based contourlet subband energy feature from the sMRI image for Alzheimer's disease classification. IEEE/ACM Transactions on Computational Biology and Bioinformatics, 19(3): 1627-1639. https://doi.org/10.1109/tcbb.2021.3051177

[17] Feng, J., Zhang, S.W., Chen, L., Xia, J., Alzheimer's Disease Neuroimaging Initiative. (2021). Alzheimer's disease classification using features extracted from nonsubsampled contourlet subband-based individual networks. Neurocomputing, 421: 260-272. https://doi.org/10.1016/j.neucom.2020.09.012

[18] Bhasin, H., Agrawal, R.K., Alzheimer's Disease Neuroimaging Initiative. (2020). A combination of 3-D discrete wavelet transform and 3-D local binary pattern for classification of mild cognitive impairment. BMC Medical Informatics and Decision Making, 20: 1-10. https://doi.org/10.1186/s12911-020-1055-x

[19] Francis, A., Pandian, I.A. (2021). Early detection of Alzheimer's disease using local binary pattern and convolutional neural network. Multimedia Tools and Applications, 80(19): 29585-29600. https://doi.org/10.1007/s11042-021-11161-y

[20] Sarwinda, D., Bustamam, A. (2016). Detection of Alzheimer's disease using advanced local binary pattern from hippocampus and whole brain of MR images. In 2016 International Joint Conference on Neural Networks (IJCNN), Vancouver, BC, Canada, pp. 5051-5056. https://doi.org/10.1109/ijcnn.2016.7727865

[21] Oppedal, K., Eftestøl, T., Engan, K., Beyer, M.K., Aarsland, D. (2015). Classifying dementia using local binary patterns from different regions in magnetic resonance images. Journal of Biomedical Imaging, 2015: 5-5. https://doi.org/10.1155/2015/572567

[22] Koh, J.E.W., Jahmunah, V., Pham, T.H., Oh, S.L., Ciaccio, E.J., Acharya, U.R., Yeong, C.H., Fabell, M.K.M., Rahmat, K., Vijayananthan, A., Ramli, N. (2020). Automated detection of Alzheimer's disease using bi-directional empirical model decomposition. Pattern Recognition Letters, 135: 106-113. https://doi.org/10.1016/j.patrec.2020.03.014

[23] Kaplan, E., Baygin, M., Barua, P.D., Dogan, S., Tuncer, T., Altunisik, E., Palmer, E.E., Acharya, U.R. (2023). ExHiF: Alzheimer's disease detection using exemplar histogram-based features with CT and MR images. Medical Engineering &Amp; Physics, 115: 103971. https://doi.org/10.1016/j.medengphy.2023.103971

[24] Reddy, K.S., Kumar, V.V., Kumar, A.S. (2017). Classification of textures using a new descriptor circular and elliptical-LBP (CE-ELBP). International Journal of Applied Engineering Research, 12(19): 8844-8853.

[25] Vimala, C., Priya, P.A. (2014). Noise reduction based on double density discrete wavelet transform. In 2014 International Conference on Smart Structures and Systems (ICSSS), Chennai, India, pp. 15-18. https://doi.org/10.1109/icsss.2014.7006177

[26] Selesnick, I.W., Baraniuk, R.G., Kingsbury, N.C. (2005). The dual-tree complex wavelet transform. IEEE Signal Processing Magazine, 22(6): 123-151. https://doi.org/10.1109/msp.2005.1550194

[27] Selesnick, I.W. (2004). The double-density dual-tree DWT. IEEE Transactions on Signal Processing, 52(5): 1304-1314. https://doi.org/10.1109/tsp.2004.826174

[28] Zhao, Q. (2021). Research on the application of local binary patterns based on color distance in image classification. Multimedia Tools and Applications, 80(18): 27279-27298. https://doi.org/10.1007/s11042-021-10996-9

[29] Srinivas, J., Qyser, A.M., Eswara Reddy, B. (2018). Classification of textures based on circular and elliptical weighted symmetric texture matrix. Periodic Engineering and Natural Sciences, 7(3.27): 593-600.

[30] Clonda, D., Lina, J.M., Goulard, B. (2004). Complex daubechies wavelets: Properties and statistical image modelling. Signal Processing, 84(1): 1-23. https://doi.org/10.1016/j.sigpro.2003.06.001

[31] Liu, J., Wang, J., Tang, Z., Hu, B., Wu, F.X., Pan, Y. (2017). Improving Alzheimer's disease classification by combining multiple measures. IEEE/ACM Transactions on Computational Biology and Bioinformatics, 15(5): 1649-1659. https://doi.org/10.1109/tcbb.2017.2731849

[32] Davatzikos, C., Tao, X., Shen, D. (2003). Applications of wavelets in morphometric analysis of medical images. In Wavelets: Applications in Signal and Image Processing X, SPIE, 5207: 435-444. https://doi.org/10.1117/12.504032

[33] Ardekani, B.A., Figarsky, K., Sidtis, J.J. (2012). Sexual dimorphism in the human corpus callosum: An MRI study using the OASIS brain database. Cerebral Cortex, 23(10): 2514-2520. https://doi.org/10.1093/cercor/bhs253

[34] Trevethan, R. (2017). Sensitivity, specificity, and predictive values: foundations, pliabilities, and pitfalls in research and practice. Frontiers in Public Health, 5: 308890. https://doi.org/10.3389/fpubh.2017.00307

[35] John, R., Kunju, N. (2018). Detection of Alzheimer's disease using fractional edge detection. Journal of Biodiversity & Endangered Species, 9(3): 2. https://doi.org/10.4172/2229-8711.1000230

[36] Padma Nanthagopal, A., Sukanesh Rajamony, R. (2012). Automatic classification of brain computed tomography

images using wavelet-based statistical texture features. Journal of Visualization, 15(4): 363-372. https://doi.org/10.1007/s12650-012-0140-3

[37] DeBrunner, V., Kadiyala, M. (1999). Texture classification using wavelet transform. In 42nd Midwest Symposium on Circuits and Systems (Cat. No.99CH36356), Cruces, NM, USA. https://doi.org/10.1109/mwscas.1999.867817

[38] Jha, D., Alam, S., Pyun, J.Y., Lee, K.H., Kwon, G.R. (2018). Alzheimer's disease detection using extreme learning machine, complex dual tree wavelet principal coefficients and linear discriminant analysis. Journal of Medical Imaging and Health Informatics, 8(5): 881-890. https://doi.org/10.1166/jmihi.2018.2381

[39] Topannavar, P.S. (2021). Rotational wavelet filters for analysis of brain MRI in detection of Alzheimer's disease. Turkish Journal of Computer and Mathematics Education (TURCOMAT), 12(6): 2817-2825. https://doi.org/10.17762/turcomat.v12i6.5789

[40] Sharma, S., Guleria, K., Tiwari, S., Kumar, S. (2022). A deep learning based convolutional neural network model with VGG16 feature extractor for the detection of Alzheimer disease using MRI scans. Measurement: Sensors, 24: 100506. https://doi.org/10.1016/j.measen.2022.100506